

# BACT-3D: A LEVEL SET SEGMENTATION APPROACH FOR DENSE MULTI-LAYERED 3D BACTERIAL BIOFILMS

J. Wang<sup>†</sup>, R. Sarkar<sup>†</sup>, A. Aziz<sup>‡</sup>, A. Vaccari<sup>†</sup>, A. Gahlmann<sup>‡</sup> and S. T. Acton<sup>†</sup>

<sup>†</sup> Department of Electrical & Computer Engineering and <sup>‡</sup> Department of Chemistry  
University of Virginia, Charlottesville, VA 22904, USA

## ABSTRACT

In microscopy, new super-resolution methods are emerging that produce three-dimensional images at resolutions ten times smaller than that provided by traditional light microscopy. Such technology is enabling the exploration of structure and function in living tissues such as bacterial biofilms that have mysterious interconnections and organization. Unfortunately, the standard tools used in the image analysis community to perform segmentation and other higher-level analyses cannot be applied naïvely to these data. This paper presents Bact-3D, a 3D method for segmenting super-resolution images of multi-leveled, living bacteria cultured *in vitro*. The method incorporates a novel initialization approach that exploits the geometry of the bacterial cells as well as an iterative local level set evolution that is tailored to the biological application. In experiments where segmentation is used as precursor to cell detection, the Bact-3D matches or improves upon the Dice score and mean-squared error of two existing methods, while yielding a substantial improvement in cell detection accuracy. In addition to providing improvements in performance over the state-of-the-art, this report also characterizes the tradeoff between imaging resolution and segmentation quality.

**Index Terms**— Level set segmentation, super-resolution, microscopy, 3D, bacteria

## 1. INTRODUCTION

The emergence of coordinated cellular behaviors is a fundamental stepping stone in the successful evolution of multicellular organisms. The multicellular lifestyle also holds the key to survival of bacterial populations even in extremely inhospitable biological niches. For example, bacteria can tolerate up to 1,000 times higher concentrations of antibiotic drugs when embedded in multicellular communities [1]. Due to this fitness advantage, a great majority of bacteria found in nature live predominantly in large multicellular communities called biofilms [2]. Biofilms containing billions of bacterial cells are abundant in the biosphere and together have an immense effect on the macroscopic environment. They support many essential ecological processes, including soil nutrient recycling

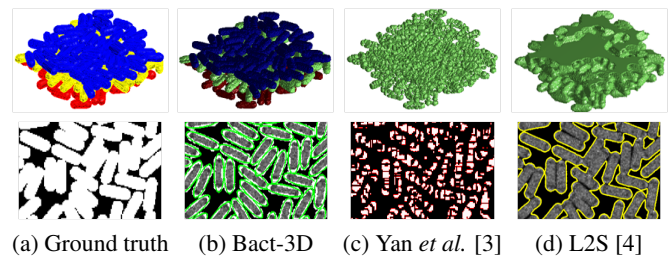


**Fig. 1:** Comparison of segmentation algorithms. The first row shows final 3D volumes reconstructed by each algorithm (different color for each layer). The second row shows the segmentation on an individual slice.

and plant growth promotion. Commensal biofilms inside the human body play an increasingly appreciated role in maintaining human health. On the other hand, undesired biofilm growth also occurs in various industrial and medical settings leading to process inefficiencies or hard to treat infectious diseases, respectively.

Understanding the behavior of individual bacteria in crowded environments is a key to controlling biofilm growth and harnessing their output for human benefit. However, our understanding of cell-to-cell intra- and inter-species cooperation or competition within pure and mixed-species biofilms is still limited. A critical barrier to progress in this field is the current inability to resolve cellular behaviors over time among many micrometer-sized bacteria in 3D biofilms [5]. Due to the diffraction-limited resolution of traditional optical microscopy, the images of individual bacterial cells strongly overlap with each other if cells are located deep within a 3D biofilm. To overcome this limitation, 3D super-resolution imaging technology [6, 7] is applied by using a lattice light sheet to excite fluorescence of a specimen. In this case, three-dimensional images at resolutions ten times smaller than that provided by traditional techniques are acquired for analysis, such as developing an effective 3D cell segmentation algorithm.

Numerous approaches for image segmentation [4, 8, 9, 10, 11, 12, 13] have been proposed over the past few decades. The level-set based segmentation model described in [8] can efficiently separate homogeneous intensity region, but fails

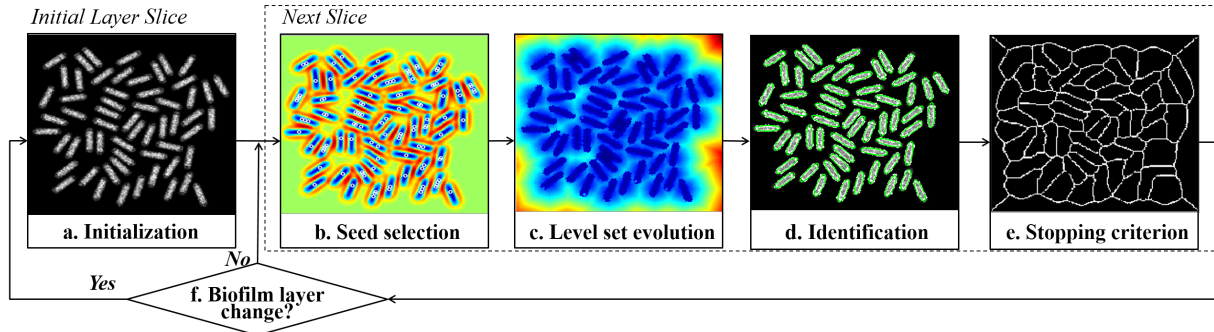


**Fig. 2:** Flow chart of Bact-3D Algorithm.

to capture the inhomogeneity inside objects to segment. Recently, the authors in [4], proposed a modified Chan-Vese technique where intensity variations within imaged regions are modeled as linear combinations of Legendre polynomial functions. While these methods are efficient in extracting regions of interest from images, they are often not able to identify multiple densely packed objects or regions as shown in Fig. 1(c-d).

In order to differentiate the individual regions of interest (bacteria in our case), algorithms which can identify and leverage small separation between regions are desired. Approaches such as [11] use the gradient flow to identify segment contours whereas a method proposed in [14] attempts to separate large segmented regions by identifying concave points along the contour. For both approaches, situations where the intensity of the regions of interest is non-homogeneous often lead to incorrect segmentation since, in these cases, multiple concave points present on the contours do not necessarily denote the presence of adjacent cells. A recent work on the segmentation of time-lapse images of bacteria was proposed in [15] where the authors presented a robust method to track bacteria in dense mono-layer flow using an iterative threshold-based approach. This method is not applicable to multi-layered bacteria biofilm, such as those we analyze in this work, where the orientation and position of the bacteria change significantly with depth of the biofilm. The segmentation algorithm presented in [3] allows to track bacterial growth in a dense multi-layered community and it is based on watershed [11]. Similarly to previous approaches, this method struggles with the detection of individual bacterial region when the intra-region density is not uniform.

In this paper we propose Bact-3D: an approach which detects and tracks individual bacteria with depth, from a densely packed multi-layered 3D volume. We exploit the idea of over-segmentation [16] to localize bacteria within each slice in the  $z$ -direction, while simultaneously propagating the background (non-bacteria) detection to the subsequent slices to retain the separability between individual bacteria. The different bacterial layers within the biofilm are identified by detecting transitions in the number of detected cells as function of slice location along the  $z$ -direction.

## 2. METHODOLOGY

In order to identify and segment the individual bacteria in 3D, we propose an approach in which we first analyze each layer and finally reconstruct the segmented 3D volume. Fig. 2 gives an overview of the methodology involved in performing slice-by-slice segmentation in a layered biofilm.

### 2.1. Dataset generation

To evaluate the accuracy of our proposed approach and to compare it to existing methods, we generated five different data sets that closely replicate the fluorescence emission from a tightly-packed cluster of bacteria, similar to those found in a microbial biofilm grown on an agarose pad.

Each data set was generated using a two-step algorithm. First, bacterial cell volumes were approximated as cylinders,  $2\text{ }\mu\text{m}$  in length and of radius  $0.5\text{ }\mu\text{m}$ , with hemispherical end caps of radius  $0.5\text{ }\mu\text{m}$ . These volumes were randomly filled with 10,000 points drawn from a spatially-uniform distribution. Cells were then randomly rotated in the  $x$ - $y$  plane and placed by a packing algorithm within  $20\text{ }\mu\text{m} \times 20\text{ }\mu\text{m}$  field of view. The algorithm shifted each cell based on its proximity to its neighbors until no overlap between adjacent cells occurred. The generated cell layer was then rotated twice in 90 degree increments to create two more cell layers that were positioned above each other and on top of the original layer. The final result closely simulates a three layer structure where each point represents an individual fluorescence emitter. In the second step, the points in each data set were convolved with a Gaussian kernel and then summed to generate light intensity values. The size and symmetry of the Gaussian kernel were chosen to closely mimic the anisotropic spatial resolution encountered experimentally:  $\sigma_x = \sigma_y = 77\text{ nm}$  and  $\sigma_z = 192\text{ nm}$ . To evaluate the performance of the algorithm as function of the instrumentation imaging resolution, two achievable super-resolutions were simulated: the first is approximately a two-fold improvement in resolution over diffraction-limited imaging (called “Resolution 1”) and the second is three times better (and is called “Resolution 2”). The first dataset was generated by utilizing a Gaussian with a kernel half the size of the diffraction limited as specified above whereas the second used a kernel one third of the

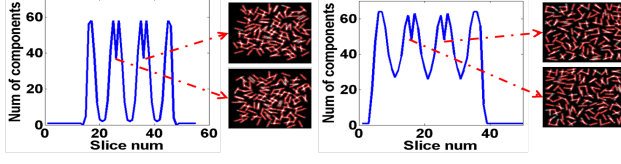


**Fig. 3:** Automated layer detection examples.

diffraction limited size.

## 2.2. Algorithm initialization

Although bacteria are densely packed, their ellipsoidal shape, due to the interaction between the distribution of fluorophores and the simulated point spread function, helps in identifying a  $z$ -plane where all the individual cells are completely separated. To automatically identify this *starting* slice we analyze the number of detected bacteria as function of slice location along the  $z$ -direction. The bacteria detection is performed by the level set method described in sec. 2.4. We take advantage of the parallel layer configuration to identify the slices belonging to each layer. As it can be seen in Fig. 3, while the number of detected cells is fairly constant within a layer, in the transition slices, the number of detected cells falls due to the mutual layer encroaching. We use these dips to identify the first and last slice of each layer. Once the *starting* slice is selected, the individual bacteria can be identified and the skeleton of the background used as a prior in the segmentation of the following slice (Fig. 2a). The algorithm, highlighted in Fig. 2(b-e) and described in the following sections, will identify ideal seeds location within each bacteria (Fig. 2b), evolve level set functions from the seed point (Fig. 2c) and determine a stopping criterion (Fig. 2 b) based on the skeleton of the background [17] (Fig. 4b).

## 2.3. Curvature-based seed selection

After smoothing the image, a set of local maxima to use as initialization seed for the level set analysis is found by evaluating the Hessian [18] of the original image and using the most negative eigenvalues to select the brightest locations with the highest curvature within each bacterium [15]. These local maxima define the seeds of the initialization contours (Fig. 4a) for the level set evolution (Fig. 2b).

## 2.4. Iterative level set evolution

The local level set method developed here is motivated by the idea of over-segmentation. In [16], the authors proposed a method for over segmentation by evolving a level set function from local uniformly spaced seeds points. In our method, we evolve the level set function from the seeds identified as discussed in sec. 2.2 and allow the contours, defined by the level set function, to evolve in a local neighborhood. The level set is evolved until it reaches a stopping criterion, obtained exploiting the prior slice segmentation result.

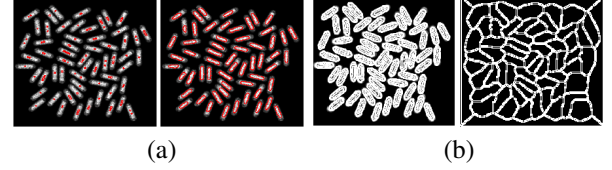


**Fig. 4:** (a) shows the initial seed selection and evolution. (b) shows the final thresholding result and skeleton determination.

The framework of level set segmentation was proposed in [19]. A signed Euclidean distance function  $\phi(x,y)$  iteratively updates the distances to the closest boundary positions at each iteration  $t$ . The object boundary is defined by the zero level set.

$$C = \{(x, y) : \phi(x, y) = 0\} \quad (1)$$

The inside of the contour is denoted by  $\phi < 0$ , while the outside is  $\phi > 0$ . Using the chain rule, the general expression for the evolution of  $\phi$  and hence the contour can be expressed as

$$\frac{\partial C}{\partial t} = VN \iff \frac{\partial \phi}{\partial t} = -V|\nabla \phi| \quad (2)$$

where  $V$  is the velocity of the evolving curve and  $N = \nabla \phi / |\nabla \phi|$  is the outward normal force. The gradient descent update for the discrete level set at each time step  $\Delta t$  is given by

$$\phi^{n+1} = \phi^n - V|\nabla \phi^n| \Delta t \quad (3)$$

To prevent the merging of evolving contours in slices where the boundaries of adjacent bacteria blur into each other due to the imaging resolution, it is critical to define a stopping criterion (where the curve evolution velocity is set to 0) that clearly separates adjacent cells. This is achieved by defining a piecewise velocity function as follows:

$$V = \begin{cases} 0 & , \text{ if SC} = 1 \\ g[1 - \epsilon\kappa] - \beta\nabla gN, & \text{ otherwise} \end{cases} \quad (4)$$

The  $V = 0$  condition effectively prevents the contours, driven by the level set evolution, from crossing the boundaries defined by the stopping criterion (SC) described in sec. 2.6. The velocity model  $V = g[1 - \epsilon\kappa] - \beta\nabla gN$  [20] represents the propagating rate of the evolving curve toward the cell boundary. In this formula,  $\kappa$  is generally the curvature forcing a slow down at the boundary areas,  $\epsilon$  and  $\beta$  are the contour smoothing and edge attracting regularization, and  $g$  is the local affinity function as defined in [16]:

$$g(x, y) = e^{-E(x,y)/\nu}, \quad E(x, y) = \frac{|\nabla I|}{G_\sigma * |\nabla I| + \gamma} \quad (5)$$

where  $\nabla I$  is the gradient of the image,  $G_\sigma$  is a smoothing kernel, and  $\gamma$  is a constant to guarantee that  $E$  will remain limited in presence of small gradients.

## 2.5. Location and orientation of individual bacteria

The final signed distance function  $\phi$  is first binarized, followed by component labeling to identify and count the number of bacteria. To extract information about the individual

	Resolution 1									Resolution 2								
	Bact-3D			Yan, et al. [3]			L2S [4]			Bact-3D			Yan, et al. [3]			L2S [4]		
	Dice	MSE	CD%	Dice	MSE	CD%	Dice	MSE	CD%	Dice	MSE	CD%	Dice	MSE	CD%	Dice	MSE	CD%
Data1	0.88	0.08	<b>100.0</b>	0.54	0.24	58.7	<b>0.89</b>	<b>0.07</b>	1.14	0.86	<b>0.08</b>	<b>100.0</b>	0.53	0.24	94.6	<b>0.87</b>	0.09	3.4
Data2	0.86	0.08	<b>100.0</b>	0.56	0.19	61.9	<b>0.88</b>	<b>0.07</b>	9.1	0.84	0.08	<b>100.0</b>	0.56	0.20	70.8	<b>0.86</b>	<b>0.07</b>	40.2
Data3	0.87	0.09	<b>100.0</b>	0.56	0.26	59.1	<b>0.89</b>	<b>0.08</b>	3.1	0.87	<b>0.08</b>	<b>100.0</b>	0.54	0.26	61.6	<b>0.88</b>	0.09	6.1
Data4	0.87	0.09	<b>99.5</b>	0.56	0.26	47.4	<b>0.89</b>	<b>0.07</b>	4.1	0.87	<b>0.08</b>	<b>99.5</b>	0.55	0.26	68.8	<b>0.88</b>	0.09	1.0
Data5	0.87	0.09	<b>99.5</b>	0.57	0.25	55.6	<b>0.89</b>	<b>0.08</b>	8.9	0.86	0.09	<b>99.7</b>	0.55	0.26	65.4	<b>0.87</b>	<b>0.09</b>	5.1

**Table 1:** Comparison of segmentation efficiency.

bacteria, the final contours of each bacterium are fitted with an ellipse ( $ax^2 + bxy + cy^2 + dx + ey + f = 0$ ) using the least-square method described in [21] with an added constraint based on our prior knowledge of the average bacterium size. Location, length, and orientation are then evaluated from the estimated conic equation parameters  $a, b, c, d, e, f$ .

### 2.6. Stopping criterion and re-initialization

Following the ellipse fitting, the elliptic contours are used to define the bacteria-background boundaries. Taking advantage of the smoothness of these boundaries, we can in turn obtain a smooth skeleton of the background region (Fig. 4b). This skeleton provides the additional stopping criterion that forces  $V = 0$  in our piecewise definition of  $V$  (4), and is used as a prior information to insure that the separation between the bacteria is maintained, even in the presence of blurred edges, during the level set evolution step in the following slice.

At the interface between layers (sec. 2.2), the skeleton from the previous slice is disregarded and a new skeleton is automatically reinitialize to conform to the location and orientation of the detected bacteria in the new layer (Fig. 2f).

## 3. EXPERIMENTAL RESULTS

The analysis and comparison with existing methods are performed on five simulated data sets, generated as described in sec. 2.1. Each slice is analyzed separately and the regions corresponding to each bacterium are joined across slices to from the final 3D volume segmentation (Fig. 1b). To separate the individual layers in the  $z$ -direction, the slices corresponding to the detected layer transition are set to zero value.

We quantitatively compared our results with two published algorithms: *single cell tracking* by Yan, et al. [3] and *L2S* [4]. Yan’s single cell tracking method is implemented using the available open source code where the value of 10 used in the watershed algorithm was empirically chosen to optimize the output. For L2S, we used the published code in a slice-by-slice implementation and then merged all the segmented slices along the  $z$ -direction to achieve the final 3D volume. We evaluate the performance of these three methods quantitatively using the *Dice coefficient*, *mean squared error* and *cell detection accuracy* (Table. 1). The Dice coefficient compares the similarity between two sets: the ground truth  $V_g$  and the detected  $V_t$  volume, and it is evaluated by  $\frac{2|V_g \cap V_t|}{|V_g| + |V_t|}$ , where  $|\cdot|$  denotes the cardinality of the corresponding set, and varies

between 0 to 1 with unity indicating optimal segmentation. Mean squared error ( $MSE = \|V_g - V_t\|_2^2$ ), measures the average squared errors between ground truth  $V_g$  and detected  $V_t$  volumes. The MSE is normalized by the total number of pixels in the volume. The cell detection accuracy (CD) determines how many cells are segmented and identified  $N_t$  compared with the actual number in the ground truth volume  $N_g$ . We define this measure similarly to the Dice coefficient:  $CD = \frac{2 \min(N_g, N_t)}{N_g + N_t}$ . The ground truth was defined, identically for all the resolutions, as the solid volumes occupying the simulated bacterial cells before the blurring by the Gaussian kernel. The value was set to unity for the inside of the cells and zero for the outside. The same index-type function was used for the detections obtained by the three methods allowing for a direct comparison.

Due to the high over-segmentation results, the single cell tracking method [3] has no evident advantages when compared with the two other methods. Although L2S [4] shows a slightly better performance in the Dice and MSE metrics, when considering the accuracy in single cell identification (CD), the proposed Bact-3D shows a significant advantage with an average accuracy of 99.81%. Bact-3D output provides us not only with a clear 3D reconstruction of the layered biofilm (Fig. 1, row 1) but also with the ability to identify each individual bacterium allowing the extraction of statistical information about location, size and orientation.

We also applied the same experiments on the real datasets. Although the cell identification ratio degraded to about 50%, the method still showed significant performance in localizing individual bacteria. The reduction in CD was mainly caused by the difficulty in identifying a good separation slice with which the stopping criterion can be computed.

## 4. CONCLUSION

Overall, a segmentation approach based on geometric active contour for dense multi-layered bacterial biofilms is presented. The segmentation exploits super-resolution data achieved via novel microscopy. With quantitatively effective segmentation and identification performance of individual bacterium in biofilms, Bact-3D provides a robust precondition for tracking [22] the bacteria growth in future work. Meanwhile, we will extend our local level set algorithm to general multi-layered real data sets with noise to increase the robustness of our method.

## 5. REFERENCES

- [1] Q. Zhang, G. Lambert, D. Liao, et al., "Acceleration of emergence of bacterial antibiotic resistance in connected microenvironments," *Science*, vol. 333, no. 6050, pp. 1764–1767, 2011.
- [2] L. Hall-Stoodley, J.W. Costerton, and P. Stoodley, "Bacterial biofilms: from the natural environment to infectious diseases," *Nature reviews microbiology*, vol. 2, no. 2, pp. 95–108, 2004.
- [3] J. Yan, A.G. Sharo, H. A. Stone, N. S. Wingreen, and B. L. Bassler, "Vibrio cholerae biofilm growth program and architecture revealed by single-cell live imaging," *Proceedings of the National Academy of Sciences*, vol. 113, no. 36, pp. E5337–E5343, 2016.
- [4] S. Mukherjee and S. T. Acton, "Region based segmentation in presence of intensity inhomogeneity using legendre polynomials," *IEEE Signal Processing Letters*, vol. 22, no. 3, pp. 298–302, 2015.
- [5] C. D. Nadell, K. Drescher, and K. R. Foster, "Spatial structure, cooperation and competition in biofilms," *Nature Reviews Microbiology*, 2016.
- [6] B. C. Chen, W. R. Legant, K. Wang, et al., "Lattice light-sheet microscopy: Imaging molecules to embryos at high spatiotemporal resolution," *Science*, vol. 346, no. 6208, pp. 1257998, 2014.
- [7] D. Li, L. Shao, B. C. Chen, et al., "Extended-resolution structured illumination imaging of endocytic and cytoskeletal dynamics," *Science*, vol. 349, no. 6251, pp. aab3500, 2015.
- [8] T. F. Chan and L. A. Vese, "Active contours without edges," *IEEE Transactions on Image Processing*, vol. 10, no. 2, pp. 266–277, 2001.
- [9] X. Han, C. Xu, and J.L. Prince, "A topology preserving level set method for geometric deformable models," *IEEE Transactions on Pattern Analysis and Machine Intelligence*, vol. 25, no. 6, pp. 755–768, June 2003.
- [10] C. Xu and J. L. Prince, "Snakes, shapes, and gradient vector flow," *IEEE Transactions on Image Processing*, vol. 7, no. 3, pp. 359–369, Mar 1998.
- [11] L. Vincent and P. Soille, "Watersheds in digital spaces: an efficient algorithm based on immersion simulations," *IEEE Transactions on Pattern Analysis and Machine Intelligence*, vol. 13, no. 6, pp. 583–598, 1991.
- [12] R. Sarkar, S. Mukherjee, and S. T. Acton, "Dictionary learning level set," *IEEE Signal Processing Letters*, vol. 22, no. 11, pp. 2034–2038, 2015.
- [13] S. T. Acton and N. Ray, "Biomedical image analysis: Segmentation," *Synthesis Lectures on Image, Video, and Multimedia Processing*, vol. 4, no. 1, pp. 1–108, 2009.
- [14] X. Bai, C. Sun, and F. Zhou, "Touching cells splitting by using concave points and ellipse fitting," in *2008 Digital Image Computing: Techniques and Applications*, 2008, pp. 271–278.
- [15] S. K. Sadanandan, Ö. Baltekin, K. E. G. Magnusson, et al., "Segmentation and track-analysis in time-lapse imaging of bacteria," *IEEE Journal of Selected Topics in Signal Processing*, vol. 10, no. 1, pp. 174–184, 2016.
- [16] A. Levinshtein, A. Stere, K. N. Kutulakos, D. J. Fleet, S. J. Dickinson, and K. Siddiqi, "Turbopixels: Fast superpixels using geometric flows," *IEEE Transactions on Pattern Analysis and Machine Intelligence*, vol. 31, no. 12, pp. 2290–2297, 2009.
- [17] K. Siddiqi, S. Bouix, A. Tannenbaum, and S. W. Zucker, "The hamilton-jacobi skeleton," in *Proceedings of the Seventh IEEE International Conference on Computer Vision*, 1999, vol. 2, pp. 828–834.
- [18] J. A. Thorpe, *Elementary topics in Differential Geometry*, Springer, 1994.
- [19] S. Osher and J. Sethian, "Fronts propagating with curvature-dependent speed: algorithms based on hamilton-jacobi formulations," *Journal of Computational Physics*, vol. 79, pp. 12–49, 1988.
- [20] C.O. Solorzano, R. Malladi, S.A. Lelievre, and S.J. Lockett, "Segmentation of nuclei and cells using membrane related protein markers," *Journal of Microscopy*, vol. 201, pp. 404415, 2001.
- [21] A. W. Fitzgibbon, M. Pilu, and R. B. Fisher, "Direct least squares fitting of ellipses," *IEEE Trans. Pattern Anal. Mach. Intell.*, vol. 21, no. 5, pp. 476–480, 1996.
- [22] S. T. Acton and N. Ray, "Biomedical image analysis: tracking," *Synthesis Lectures on Image, Video, and Multimedia Processing*, vol. 2, no. 1, pp. 1–152, 2006.